Available online at website: https://journal.bcrec.id/index.php/bcrec

Bulletin of Chemical Reaction Engineering & Catalysis, 21 (2) 2026, 244-261

Review Article

Modification Strategies of Copper Molybdate-based Photocatalysts for Degradation of Organic Compounds in Wastewater: A Mini Review

Hamidah binti Abdullah[1], Rohayu binti Jusoh[1], Wahaizad bin Safie[2], Ricca Rahman binti Nasaruddin[3], Maksudur Rahman Khan[4], Md Noor bin Arifin[1*]

[1]*Faculty of Chemical and Process Engineering Technology, Universiti Malaysia Pahang Al-Sultan Abdullah, 26300 Gambang, Pahang, Malaysia.*
[2]*Faculty of Manufacturing and Mechatronic Engineering Technology, Universiti Malaysia Pahang Al-Sultan Abdullah, 26600 Pekan, Pahang, Malaysia.*
[3]*Department of Biotechnology Engineering, Kulliyyah of Engineering, International Islamic University, 50728 Kuala Lumpur, Malaysia.*
[4]*Petroleum and Chemical Engineering Programme, Faculty of Engineering, Universiti Teknologi Brunei, Jalan Tungku Link Gadong, BE1410, Brunei Darussalam.*

Received: 6th January 2026; Revised: 14th January 2026; Accepted: 15th January 2026
Available online: 28th January 2026; Published regularly: August 2026

Abstract

Visible-light photocatalysis has emerged as a sustainable tertiary-treatment option. Within this arena, copper molybdate ($CuMoO_4$) is attractive because of its narrow bandgap enables direct solar harvesting while relying on earth-abundant elements. Yet pristine $CuMoO_4$ suffers from low surface area (< 10 m^2/g), rapid electron-hole recombination and Cu^{2+} photocorrosion, which curb quantum yields and raise secondary-pollution concerns. This mini review critically synthesizes research published between 2019 and 2025 on strategies devised to surmount these limitations. Four major areas are surveyed: (i) morphology engineering that multiplies active-site density and deepens light scattering; (ii) plasmonic or single-atom noble-metal decoration that extends spectral response and accelerates interfacial charge separation via localized surface plasmon resonance; (iii) band-gap and defect modulation through doping or oxygen-vacancy creation, narrowing band gap and introducing long-lived trapping states, and (iv) construction of p-n heterojunctions (e.g., $ZnO/CuMoO_4$, graphitic carbon nitride/copper molybdate ($g\text{-}C_3N_4/CuMoO_4$) that yield order-of-magnitude rate enhancements by spatially separating redox half-reactions. The synthesis approaches, from hydrothermal and co-precipitation to thermal-decomposition and solid-state reactions directly influence crystallinity, morphology and defect chemistry, with optimal hydrothermal conditions (180 °C, 10 h) producing high-purity α-$CuMoO_4$ microspheres and oxygen-vacancy-rich Cu-rich phases delivering up to a 0.5 eV bandgap reduction. Emphasis is placed on correlating structural descriptors with pollutant-mineralization kinetics and on emerging green-synthesis trends. Remaining challenges and research priorities including stability against Cu leaching, scalable fabrication and in-situ mechanistic probes are highlighted to guide future catalyst design.

Copyright © 2026 by Authors, Published by BCREC Publishing Group. This is an open access article under the CC BY-SA License (https://creativecommons.org/licenses/by-sa/4.0).

Keywords: Visible-light Photocatalysis; Copper Molybdate; Morphology Engineering; Defect Modulation; p-n Heterojunctions

How to Cite: Abdullah, H. b., Jusoh, R. b., Safie, W. b., Nasaruddin, R. R. b., Khan, M. R., Arifin, M. N. b. (2026). Modification Strategies of Copper Molybdate-based Photocatalysts for Degradation of Organic Compounds in Wastewater: A Mini Review. *Bulletin of Chemical Reaction Engineering & Catalysis*, 21 (2), 244-261. (DOI: 10.9767/bcrec.20627)

Permalink/DOI: https://doi.org/10.9767/bcrec.20627

1. Introduction

The presence of biologically active and chemically resilient organic pollutants in municipal and industrial wastewater has become a critical environmental challenge over the past decade, with pharmaceuticals, pesticides, endocrine-disrupting chemicals and synthetic dyes now being detected worldwide in final effluents [1]. Persistence arises from aromaticity, halogenation and other substituents that confer resistance to biodegradation and direct photolysis, so that even advanced biological plants hardly

* Corresponding Author.
Email: noormd@umpsa.edu.my (M.N. Arifin)

remove many antibiotics and hormones [2]. Toxicological studies show that 17-α-ethinylestradiol can trigger intersex conditions in fish at 1 to 5 ng/l and sulfonamide antibiotics inhibit algal growth at only a few µg/l, demonstrating that trace concentrations are sufficient to impair aquatic ecosystems [3,4]. Visible-light photocatalysis is therefore regarded as a promising tertiary treatment because roughly 45 % of the solar spectrum lies in the 400 - 700 nm range that can be harvested without artificial irradiation [5,6]. Among recently explored semiconductors, $CuMoO_4$ has attracted attention for its narrow 1.9-2.0 eV band gap [7], cost effective [8] and its ability to exist in various states [9], positioning it as a candidate for sustainable solar-based advanced oxidation processes.

Although benchmark materials, such as anatase TiO_2 with a band gap of 3.2 eV [10] and ZnO, can fully mineralize model dyes under ultraviolet lamps, their activity drops sharply under simulated sunlight because only about 5 % of terrestrial irradiance is UV [10,11]. By contrast, $CuMoO_4$ degraded rhodamine-B (RhB) 1.39 times faster than N-doped TiO_2 and achieved 1.53-fold higher total organic carbon removal under the same visible-light conditions [7]. A hydrothermal "pebble-stone" $CuMoO_4$ removed 94.7 % of methylene blue (MB) in 50 min, outperforming pristine ZnO and matching the best bismuth vanadate ($BiVO_4$) reports under identical photon flux [12]. Nevertheless, intrinsic limitations remain. The conduction-band edge of $CuMoO_4$ (-0.3 to 0.4 V vs Normal Hydrogen Electrode (NHE)) is only marginally negative to the $O_2/O_2^{\cdot-}$ couple, restricting its reduction power, while the valence band (+1.5 to +1.7 V) is insufficient to oxidize water to hydroxyl radicals [7]. Consequently, superoxide anion becomes the dominant reactive oxygen species generated, which can slow mineralization of highly halogenated or polyaromatic contaminants [13]. In addition, $CuMoO_4$ photocatalysts synthesized by combustion or solid-state routes exhibit specific surface areas below 10 m^2/g, leading to poor adsorption and pronounced particle agglomeration that retard interfacial kinetics [14]. Moreover, as with other Cu-oxides, prolonged irradiation can trigger photocorrosion and Cu^{2+} leaching, posing secondary pollution risks if protective measures are not implemented [15].

To address these drawbacks, researchers have investigated a spectrum of modification strategies. Comparative studies in the recent literature reveal distinct trade-offs between these modification approaches. While elemental doping, such as the incorporation of yttrium (Y) into the $CuMoO_4$ lattice, has been shown to effectively narrow the bandgap from 1.44 eV to 1.39 eV and increase charge migration by five-fold [16], it is often limited by the thermodynamic solubility of the dopant and potential leaching during long-term operation [17]. In contrast, the construction of heterojunctions generally offers superior stability and charge separation efficiency. For instance, recent work on Type-II heterojunctions, such as $CuMoO_4/Bi_2S_3$, demonstrated a degradation efficiency of 98% for organic dyes, nearly double that of pure $CuMoO_4$ (53%) under identical solar irradiation [18]. Furthermore, advanced S-scheme heterojunctions like $ZnMoO_4/ZnIn_2S_4$ have achieved hydrogen evolution rates over 10 times higher than their individual components by preserving high-redox-potential charge carriers, a feat that simple morphology engineering alone cannot achieve [19]. Thus, while morphology control provides necessary surface active sites, integrating it with heterojunction engineering represents the current frontier for maximizing quantum efficiencies in molybdate-based photocatalysts.

$ZnO/CuMoO_4$ and $g\text{-}C_3N_4/CuMoO_4$ heterojunctions lengthen charge-carrier lifetimes and extend spectral utilization, enabling 92 % MB removal in 70 min and seven-fold acceleration of tetracycline degradation relative to the single components [20]. Morphology engineering ranging from 45 m^2/g nanorods to hollow urchin-like microspheres with multiplies active-site density and augments light scattering for deeper photon capture [21]. Against this backdrop, a comprehensive synthesis of literature on $CuMoO_4$ modification is urgently needed to guide rational materials design and accelerate translation from bench to practice. A summary of modification techniques is presented in Figure 1. The present mini review therefore collates advances published

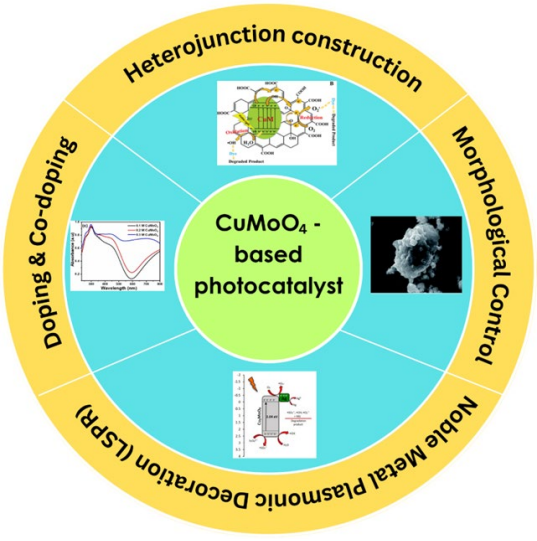

Figure 1. Schematic illustration of the four primary modification strategies for $CuMoO_4$-based photocatalysts reviewed in this work: heterojunction construction, morphological control, noble metal plasmonic decoration (LSPR), and doping/co-doping.

Copyright © 2026, ISSN 1978-2993

between 2019 and 2025, critically examines how each structural or compositional intervention influences light harvesting, charge separation, interfacial redox chemistry and concludes with prioritized research directions.

2. Photocatalytic Degradation Mechanisms over Copper Molybdate Photocatalyst

$CuMoO_4$ has long been recognized as a photochemically versatile oxide whose mixed-metal framework couples a narrow visible-light band gap with a redox-flexible Cu^{2+}/Cu^{+} sub-lattice. In its most studied triclinic α-phase, whose crystal growth and properties were first detailed in 1968 [22] and structure determined shortly thereafter [23], the valence band is dominated by O 2p states that hybridize with Mo 4d and Cu 3d orbitals. The conduction band is mostly made up of Mo 4d orbitals, making the material with appreciable absorption of the solar spectrum [15].

To better understand the mechanism of photocatalytic degradation of organic molecules over $CuMoO_4$ photocatalyst, a study was chosen to demonstrate the steps and details of the analytical results such as radicals and mass spectrometry experiments [21]. MB was commonly selected as a benchmark contaminant because its chromophore structure is highly sensitive to radical attack, allowing precise tracking of reactive oxygen species [23,24]. Upon light irradiation, $CuMoO_4$ photocatalyst generate superoxide radicals ($O_2^{\cdot-}$), hydroxyl radicals (·OH), electrons (e^-) and holes (h^+), which can oxidize organic contaminants to CO_2 and H_2O. To elucidate which of these species drive MB degradation by $CuMoO_4$ photocatalyst, trapping experiments were conducted in an aqueous MB suspension containing 0.3 M $CuMoO_4$, in the presence of light and specific quenchers; benzoquinone (BQ) for $O_2^{\cdot-}$, isopropyl alcohol (IPA) for ·OH, silver nitrate ($AgNO_3$) for e^- and disodium ethylenediaminetetraacetate (EDTA-2Na) for h^+ and the experiments were monitored spectrophotometrically.

The inhibition by BQ and IPA indicates that photogenerated superoxide and hydroxyl radicals are the main oxidizing agents, while the minimal impact of $AgNO_3$ and EDTA-2Na demonstrates that electrons and holes play a secondary role. These findings confirm that indirect photocatalysis via $O_2^{\cdot-}$ and ·OH is the dominant pathway for MB mineralization, consistent with reports in the literature and, together with the band-edge positions of 0.3 M $CuMoO_4$ photocatalyst, support the proposed mechanism [21] for charge separation and subsequent photocatalytic degradation of MB under sunlight irradiation, as follows:

$$CuMoO_4 + h\nu \rightarrow e^- + h^+ \quad (1)$$

$$e^- + O_2 \rightarrow O_2^{\cdot-} \quad (2)$$

$$(H_2O \leftrightarrows H^+ + OH^-) + h^+ \rightarrow H^+ + {\cdot}OH \quad (3)$$

$$MB + O_2^{\cdot-}/{\cdot}OH/h^+ \rightarrow \text{intermediates} \rightarrow \text{degradation products} \quad (4)$$

Liquid-chromatography mass spectrometry (LC-MS) revealed several transient species (Figure 2(a)), whose molecular structures were assigned from their characteristic mass-to-charge ratios. Under sunlight irradiation, MB (MB, m/z = 320) undergoes a stepwise photocatalytic degradation in water, generating a succession of

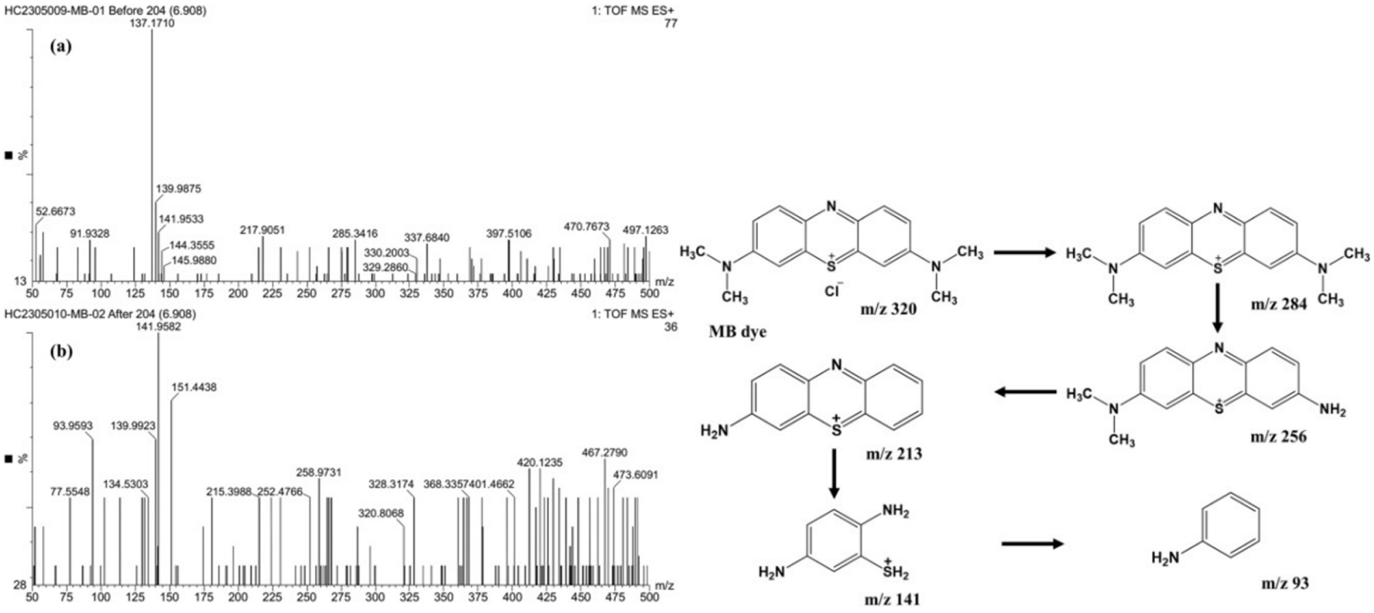

Figure 2. Liquid-chromatography mass spectrometry (LC-MS) analysis of Methylene Blue (MB) degradation. Panels show a) the mass spectrum of the initial MB dye (m/z = 320), b) the spectrum of degradation intermediates after irradiation, and c) the proposed degradation pathway involving ring opening and bond cleavage steps [24].

Copyright © 2026, ISSN 1978-2993

increasingly simple, environmentally benign intermediates. The pathway outlined in (Figure 2(b)), begins with rupture of the N=N double bond, followed by benzene-ring opening and sequential cleavage of C-N, C-C and finally C-S bonds that connect the aromatic core to its sulfonate substituents. Together these transformations account for the complete mineralization of MB into harmless end-products.

3. Modification Strategies of $CuMoO_4$-based Photocatalysts

$CuMoO_4$ possesses an ability as a semiconductor to photodegrade organic dyes, but its baseline activity leaves room for improvement. To enhance performance and better utilize solar spectrum, various modification strategies have been developed. Below, we review key modification approaches, from morphology control to heterojunction formation, as explicitly described in the literature, along with their impacts on photocatalytic degradation of persistent organics.

3.1 Morphological Control

Controlling the crystallite size and shape of $CuMoO_4$ can influence its surface area, light absorption and reactive facet exposure [25]. Hydrothermal temperature tuning is one of the effective routes [26]. It was observed that raising the hydrothermal synthesis temperature to 200 ^oC yielded $CuMoO_4$ particles that were rounded and tiny (See Figure 3 (a)), indicating a temperature-directed refinement of primary crystallites [7]. The rounding effect at higher temperature was correlated with improved photocatalytic efficiency with the optimum temperature at 180 ^oC, due to more uniform morphology and phase purity.

Figure 3 (b) reveals that pristine $CuMoO_4$ forms granular aggregates that coalesce into dense clusters. Extending the hydrothermal treatment gradually smooths these grains, yielding increasingly rounded particles with time. Meanwhile, a sonochemical synthesis has shown an ability to produce ultra-small $CuMoO_4$ nanostructures. $CuMoO_4$ was prepared via a surfactant-free sonochemical route, resulting in roughly spherical nanoparticles from 50 to 55 nm in diameter [27]. The scanning electron microscopy (SEM) images confirmed the particles to be round, about 50-55 nm in size. These nanocrystals showed a higher photocatalytic degradation of methyl orange, close to 72 % under UV in 60 min, compared to bulk $CuMoO_4$, which the author attributes to the favourable nanoscale morphology (high surface-to-volume ratio). Tailoring $CuMoO_4$ morphology, via hydrothermal or sonochemical method can be considered as an accessible modification strategy to expose more active sites. However, morphology alone may yield only moderate activity gains, for example through incremental increase in dye removal, and often needs to be combined with other modifications for substantial improvements.

3.2 Noble-Metal Plasmonic Decoration (LSPR)

Loading of noble metals introduces localized surface plasmon resonance (LSPR) effects that extend light absorption into the visible range and promote charge separation [28]. Cu_2MoO_4 was decorated with Ag nanoparticles (Ag/Cu_2MoO_4) and demonstrated plasmon-enhanced visible-light harvesting [29], confirmed by the X-ray photoelectron spectroscopy (XPS) analysis. Under visible illumination, the Ag/Cu_2MoO_4 composite achieved 99.7 % degradation of malachite green (MG) in 50 min, whereas bare Cu_2MoO_4 reached 83.6 % within the same testing period. This performance can be attributed to the LSPR of Ag. The Ag-decorated catalyst exhibited strong visible-light absorption due to collective oscillation of Ag conduction electrons, which accelerates the separation between the generated e^- and h^+ in $CuMoO_4$, as depicted in Figure 4.

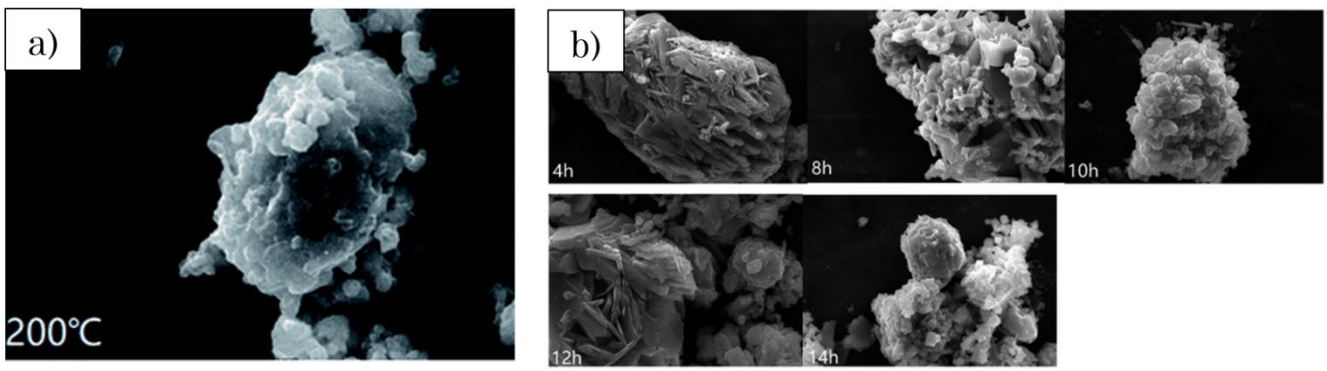

Figure 3. SEM micrographs illustrating the morphological evolution of $CuMoO_4$ synthesized via the hydrothermal method with a) shows the effect of reaction temperature (up to 200 ^oC for 10 hours) leading to particle rounding, and b) shows the effect of reaction time (4 to 14 hours at 180 ^oC) on grain smoothing and cluster formation [7].

Copyright © 2026, ISSN 1978-2993

Furthermore, electrochemical tests, such as electrochemical impedance spectroscopy (EIS) and photocurrent showed Ag/Cu_2MoO_4 had a smaller charge-transfer resistance and higher photocurrent than $CuMoO_4$, indicating more efficient charge separation. The Ag nanoparticles also slightly narrowed the effective band gap of Cu_2MoO_4, enabling excitation by longer wavelengths. It should be noted that noble-metal decoration introduces cost and potential stability issues [30], owing to the fact that Ag may oxidize or aggregate over time, even though it clearly improves visible-light activity. $CuMoO_4$, with < 2 wt. % Ag triples photocurrent, delivers 100 % dye removal in 50 min and retaining > 95 % activity over five cycles, providing a compelling benchmark for $CuMoO_4$ modification strategies [29].

3.3 Doping and Co-doping

Introducing additional cations or anions into $CuMoO_4$ can alter its electronic structure, create defect sites and improve catalytic performance [31]. Heteroatom doping as a solid solution has been demonstrated on $CuMoO_4$ within an $AlPO_4$ host lattice [32]. A copper-molybdate-doped aluminum phosphate, denoted $Cu_xMo_xAl_{1-x}P_{1-x}O_4$, via a solid-solution method. X-ray diffraction (XRD) and Fourier transform infrared spectroscopy (FTIR) confirmed formation of a single-phase mixed oxide with Cu and Mo substituting into the lattice structure of $AlPO_4$. Among various metal molybdate-doped $AlPO_4$ samples, the Cu-containing solid solution at x = 0.5 showed the best activity for photoreduction of nitroaniline pollutants under UV-visible light irradiation. This $CuMoO_4/AlPO_4$ composite exhibited semiconductor behavior with an expanded band gap of 4.21 eV and intense photoluminescence at 271 nm. The wide band gap and high-energy emission stem from the host $AlPO_4$ matrix, while the presence of $CuMoO_4$ imparts visible-light response and catalytic sites. Thus, by co-doping Cu and Mo into $AlPO_4$, a new heterostructure was achieved where the combination of $CuMoO_4$ photocatalytic functionality and $AlPO_4$ stability yield a robust UV–visible active catalyst.

In addition to foreign dopants, intrinsic Cu enrichment in $CuMoO_4$ itself can also introduce beneficial defects [24]. Cu precursor concentration (0.1, 0.2, 0.3 M) was varied in a thermal decomposition synthesis of $CuMoO_4$ and a systematic change was observed in the properties of the material. All samples remained phase-pure $CuMoO_4$, but increasing Cu content led to enlarged crystallite size, from 41 nm to 50 nm, when increased from 0.1 M to 0.3 M respectively, and notable electronic modifications. Specifically, the band gap of $CuMoO_4$ narrowed from 1.97 eV (0.1 M) to 1.44 eV (0.3 M). This 0.5 eV band gap reduction implies that excess Cu created mid-gap impurity levels or defect states [33]. Additional Cu atoms likely occupy interstitial or substitutional sites in the MoO_4 lattice, which alter the normal lattice structure and introduce electronic states between the valence and conduction bands [24]. Evidence of these defect states is a new broad absorption feature around 600 nm in the UV-visible spectra of Cu-rich samples as shown in Figure 5.

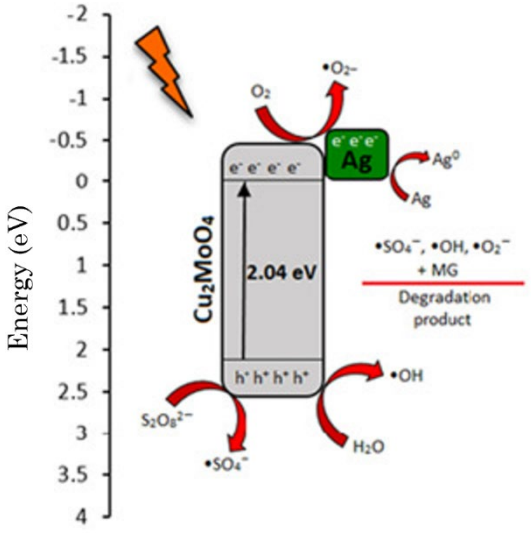

Figure 4. Schematic mechanism for the photocatalytic degradation of Malachite Green (MG) over Ag-decorated Cu_2MoO_4. The diagram highlights the Localized Surface Plasmon Resonance (LSPR) effect of Ag nanoparticles, which extends visible-light absorption and accelerates electron-hole separation [29].

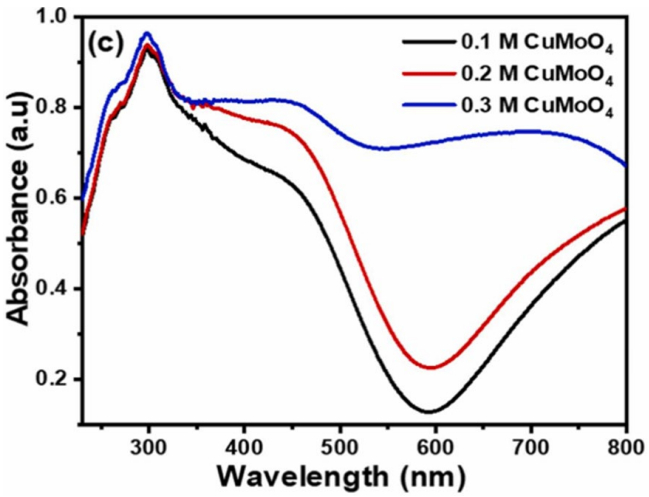

Figure 5. UV–visible absorbance spectra of $CuMoO_4$ nanoparticles synthesized with varying copper precursor concentrations (0.1-0.3 M). Note the emergence of a broad absorption feature around 600 nm and the narrowing of the band gap (from 1.97 to 1.44 eV) in the Cu-rich 0.3 M sample, attributed to oxygen-vacancy induced defect states [24].

Copyright © 2026, ISSN 1978-2993

This 600 nm feature was attributed to a plasmon-like resonance of conduction-band electrons in oxygen-deficient $CuMoO_4$. In other words, Cu excess doping induced oxygen vacancies or Cu^0 nanoclusters that give a LSPR (analogous to noble metals) at 600 nm [34]. Such defects also improved charge carrier dynamics [35]. The 0.3 M $CuMoO_4$ showed much lower photoluminescence intensity (i.e. reduced electron-hole recombination) than the 0.1 M sample. Consequently, the photocatalytic mineralization of MB under sunlight was highest for the 0.3 M $CuMoO_4$ with complete mineralization due to the increased charge-carrier density and suppressed e^-/h^+ recombination from these introduced defect states. This strategy of intrinsic doping is facile by simply varying the precursor stoichiometry, but one must ensure that no secondary phases appear via XRD measurement, showed no impurity peaks up to 0.3 M Cu [36]. Properly controlled, defect engineering via Cu stoichiometry can significantly enhance visible-light absorption and photocatalytic efficiency of $CuMoO_4$.

3.4 Heterostructure Construction

Forming heterostructures by coupling $CuMoO_4$ with other materials is a prominent strategy to improve charge separation and extend light absorption. Heterojunctions can create internal electric fields that drive photogenerated electrons and holes into separate phases, thereby reducing recombination [37]. We discuss three sub-categories: carbon-based hybrids, binary oxide p–n junctions, and 2D carbon allotrope coupling. Each approach explicitly appears in the literature with demonstrated performance gains. Recent high-impact reviews [38,39] emphasize that unlike conventional Type-II systems, advanced Z-scheme and S-scheme configurations are critical for maintaining high redox potentials in narrow-bandgap semiconductors like molybdates.

3.4.1 Carbon-based hybrids

Graphene-family carbon materials are excellent conductive supports that can accept electrons and increase adsorptive interactions [40]. Graphene oxide-copper molybdate (GO-$CuMoO_4$) nanocomposites was synthesized via ultrasonication and reflux methods. In this 2D/particle hybrid, $CuMoO_4$ nanoparticles were dispersed on GO sheets [41]. The GO- $CuMoO_4$ composite with an optimized GO:$CuMoO_4$ ratio of 2:1 achieved 99 % MB degradation in 32 min under visible light. Its apparent rate constant (0.094/min) was over 30 times higher than that of pure $CuMoO_4$ (0.0029/min, only 30 % degradation in 140 min). However, it is noted that this performance still requires enhancement when compared to 93 % of MB degradation within 13 min by GO/TiO_2 [42]. The GO plays a key role as a p-type semiconductor [43] with abundant oxygenated groups and GO sheets serve as electron acceptors and dispersants for $CuMoO_4$ [44]. Photogenerated electrons from $CuMoO_4$ transfer to GO, where they react with dissolved O_2 to produce superoxide ($O_2^{\cdot-}$) radicals. Meanwhile, the photogenerated holes remain on $CuMoO_4$ and oxidize water or OH^- to form ·OH radicals. This charge separation mechanism as illustrated in Figure 6 leads to an abundance of reactive radicals on GO-$CuMoO_4$, whereas pure $CuMoO_4$ suffered rapid electron-hole recombination.

Additionally, the large surface area and functional groups of GO improved dye adsorption and provided more reactive interfaces [45]. It was observed that increasing GO content enhanced activity up to an optimal point with 2:1 of GO: GO-$CuMoO_4$ ratio, beyond which excess GO might shield light or recombine charges. In summary, the GO-$CuMoO_4$ 2D/0D composite demonstrates how carbon hybrids can dramatically boost photocatalytic efficiency by combining the light absorption of $CuMoO_4$ with charge-carrier trapping of GO and pollutant adsorption abilities.

Graphitic carbon nitride (g-C_3N_4) is a visible-light-active 2D semiconductor with a band gap of 2.7 eV [46], was deployed to form a heterojunction formation with $CuMoO_4$ nanoflowers [47]. The g-C_3N_4/$CuMoO_4$ composite was synthesized via a one-pot solvothermal method. Electron microscopy revealed $CuMoO_4$ crystallites (10-15 nm petals) intimately anchored on the g-C_3N_4 layers. The g-C_3N_4/$CuMoO_4$ heterostructure exhibited outstanding photocatalytic degradation efficiencies with 98 % of RhB and 97 % of ciprofloxacin antibiotic were decomposed in 35

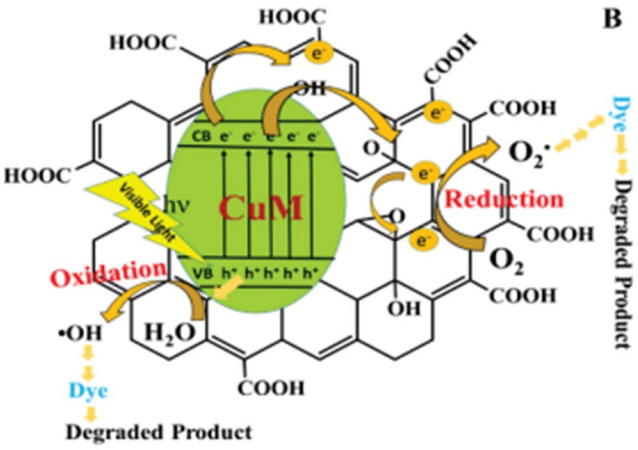

Figure 6. Schematic representation of charge separation in graphene oxide (GO)-$CuMoO_4$ nanocomposites. Photogenerated electrons transfer from $CuMoO_4$ to the GO sheets (acting as electron acceptors) to form superoxide radicals, while holes remain on $CuMoO_4$ to generate hydroxyl radicals, thereby suppressing recombination [41].

Copyright © 2026, ISSN 1978-2993

and 60 min, respectively, under visible-light illumination. These results surpassed the performance of pure g-C_3N_4 or $CuMoO_4$ alone. The superior performance of g-C_3N_4/$CuMoO_4$ is attributed to formation of heterojunction charge transfer mechanism. Upon light excitation, electrons from the conduction band (CB) of $CuMoO_4$ recombine with holes from the valence band (VB) of g-C_3N_4 at the interface, effectively leaving behind strong oxidation holes in $CuMoO_4$ (VB) and strong reduction electrons in g-C_3N_4 (CB). This direct mechanism preserves the high redox power of both semiconductors, unlike a conventional Type-II heterojunction. Consistent with the scavenger protocols described in Section 2, trapping experiments on the composite confirmed that ·OH and $O_2^{\cdot-}$ remain the primary active species, but with significantly enhanced yield due to the Z-scheme spatial separation of charge carriers. Additionally, g-C_3N_4/$CuMoO_4$ showed significantly reduced photoluminescence and a higher photocurrent than either component, reflecting efficient charge separation. The composite was stable over 5 cycles with negligible activity loss.

In summary, the g-C_3N_4/$CuMoO_4$ heterojunction exemplifies a synergistic modification with $CuMoO_4$ extending the visible absorption of g-C_3N_4 into deeper wavelengths, while g-C_3N_4, with its conductive π-structure shuttles electrons away [48]. One limitation is that the synthesis requires careful control to achieve intimate contact between phases. Otherwise, charge transfer may be insufficient [49]. Nevertheless, this g-C_3N_4/$CuMoO_4$ heterojunction strategy is a powerful way to leverage the strength of multiple semiconductors strengths in one system.

3.4.2 p–n heterojunctions

Coupling $CuMoO_4$ with metal-oxide semiconductor can form a classic p-n junction, facilitating charge separation via the built-in electric field at the interface [50]. ZnO/$CuMoO_4$ composite was fabricated using a green hydrothermal method with Bambusa vulgaris leaf extract [51]. Pure ZnO is n-type semiconductor with a band gap, E_g of 3.2 eV, primarily absorbs UV light [52], but when coupled with $CuMoO_4$, the ZnO/$CuMoO_4$ composite showed a broadened absorption into visible light, with a band gap of 2.71 eV. In this work, ZnO/$CuMoO_4$ heterojunction achieved 93.4 % dye degradation in 120 min under visible light, compared to only 55.5 % by ZnO alone. Kinetic analysis indicated a reaction rate constant 3 times higher for the ZnO/$CuMoO_4$ composite than the bare ZnO.

The enhancement can be explained by two factors, on account of enlarged light absorption by the presence of $CuMoO_4$ that enabled utilization of visible wavelengths [7] that ZnO cannot absorb and suppressed charge recombination [50]. The construction of p-n junction at the ZnO/$CuMoO_4$ interface creates an internal electric field that drives photogenerated electrons from $CuMoO_4$ to the n-ZnO and holes from ZnO to the p-$CuMoO_4$ [53]. This charge separation mechanism was evidenced by the reduction of photoluminescence and higher photocatalytic efficiency ZnO/$CuMoO_4$ photocatalysts. The ZnO/$CuMoO_4$ heterostructure leveraged the complementary properties of a wide-bandgap n-type and a narrow-bandgap p-type semiconductor.

Beyond the ZnO/$CuMoO_4$ system, recent investigations have expanded to diverse metal oxide heterojunctions to overcome the limitations of single-component $CuMoO_4$. A comparative analysis of these systems reveals distinct advantages depending on the band alignment strategy employed. For instance, TiO_2/$CuMoO_4$ composites have been shown to significantly enhance photocatalytic performance through a Type-II heterojunction mechanism. In this configuration, the specific band alignment allows photogenerated electrons to transfer from the conduction band of $CuMoO_4$ to that of TiO_2, effectively suppressing charge recombination. This synergy resulted in a 4-chlorophenol degradation efficiency of 96.9 % under visible light, far surpassing pristine TiO_2 [54]. Similarly, the coupling of $CuMoO_4$ with Bi-based oxides, such as in the $CuMoO_4$/Bi_2WO_6 system, utilizes a Z-scheme or p-n junction approach to maximize redox potential. Studies indicate that such heterojunctions can achieve degradation rates for RhB that are nearly double those of the individual components by preserving the strong oxidative ability of holes in the valence band of $CuMoO_4$ while facilitating electron transport [55].

Furthermore, recent work on Co_3O_4/$CuMoO_4$ hybrid microflowers highlights the role of morphological synergy in heterojunctions. This system utilizes the p-type conductivity of Co_3O_4 to create a p-n junction with n-type $CuMoO_4$, which not only improves charge separation via an internal electric field but also lowers the activation energy for catalytic reactions. This specific coupling has demonstrated high catalytic turnover frequencies in hydrolytic applications, suggesting its versatility for complex wastewater treatments [21]. In contrast, doping strategies, such as Y-doped $CuMoO_4$, offer an alternative route by modulating the intrinsic bandgap (lowering it to 1.39 eV) and increasing charge migration five-fold without forming a secondary phase [16]. Collectively, these findings suggest that while simple heterojunctions (like TiO_2/$CuMoO_4$) are effective for general organic pollutants, more complex Z-scheme or p-n junction designs (like Bi_2WO_6/$CuMoO_4$ or Co_3O_4/$CuMoO_4$) provide superior redox capabilities for recalcitrant

Copyright © 2026, ISSN 1978-2993

compounds, dictating the choice of modifier based on the specific target pollutant.

3.5 Surface-Defect and Oxygen-Vacancy Engineering

Creating oxygen vacancies or other surface defects on $CuMoO_4$ can profoundly affect its optical absorption and catalytic sites. Unlike bulk doping in Section 3.3, this strategy focuses on generating non-stoichiometric surfaces that often exhibit color centers of F-center like behavior [21]. This phenomenon induces plasmonic absorption due to free electrons in vacancy sites and an example of such modulation is Cu-rich $CuMoO_4$ photocatalysts [24]. It was found that the $Cu_{1-x}MoO_4$ (where $x > 1$) samples contained Cu^+ or metallic Cu and had oxygen-deficient areas. These features caused a new light absorption band to appear around 600 nm.

The presence of these oxygen-vacancy-induced states extends the light absorption into the orange-red region and provides localized electronic states that can participate in redox reactions [21,56]. Unlike the bulk recombination limitations described in Section 2, these surface oxygen vacancies act as charge carrier traps that effectively prolong the lifetime of photogenerated electrons and holes [57]. In $CuMoO_4$, an appropriate concentration of oxygen vacancies can thus improve photocatalysis by increasing visible-light absorption and by capturing electrons or holes, to prevent premature recombination. However, it is critical to achieve a balance because an excessive oxygen vacancy could turn $CuMoO_4$ into a metallic, heavily carrier-damped material or create recombination centers if they aggregate [58]. Techniques to introduce surface oxygen vacancies include annealing $CuMoO_4$ in a mildly reductive atmosphere or employing vacuum UV irradiation [59].

In summary, surface-defect engineering via Cu/Mo stoichiometry changes or reduction treatments can synthesize $CuMoO_4$ with a plasmonic 600 nm band and enhanced visible-light activity. This strategy, with a proper control, complements the other modifications. For instance, one could create oxygen vacancies in situ during the formation of $CuMoO_4$ heterojunctions or doped systems to further boost performance. By explicitly introducing and characterizing such defects, for example via XPS O 1s peak shifts or electron paramagnetic resonance (EPR) signals, researchers can correlate defect density with photocatalytic rates.

Each modification strategy above offers distinct advantages and has certain limitations. Morphology control is relatively straightforward but typically yields only incremental gains, it mainly optimizes surface area and facet exposure. Noble-metal decoration introduces strong visible-light absorption and improved charge separation via LSPR, but at the cost of using precious metals and potential stability issues, namely Ag or Au leaching. Doping and co-doping can fundamentally alter the band structure of $CuMoO_4$ and create active defect sites. This can dramatically improve performance via band gap narrowing from 1.97 to 1.44 eV, but unwanted phases should be avoided. Dopants should be prevented from leaching into the solution, to align with green chemistry principles. Heterostructure construction is arguably the most impactful strategy for boosting photocatalytic efficiency. By forming p-n junction systems, researchers have achieved order-of-magnitude increases in reaction rates [51]. The composite catalysts harness broader sunlight spectrum and greatly suppress charge recombination, which is reflected in superior pollutant removal efficiencies. The trade-off is that multi-component systems can be more complex to synthesize and optimize. Finally, surface-defect engineering is an approach that can be used in tandem with any of the above. Oxygen vacancies, for example, could be introduced in a $CuMoO_4$/ZnO composite to further extend its absorption and reactivity. When comparing across strategies, heterojunction-based modifications, especially with carbon materials or coupled semiconductors stand out for achieving the highest photocatalytic rates under visible light. Table 1 shows the summary of modification strategies of $CuMoO_4$-based materials and related experimental conditions for degradation of various pollutants.

4. Synthesis Methods of Copper Molybdate-based Materials

The efficacy of $CuMoO_4$-based materials as photocatalysts is profoundly influenced by their physicochemical properties, such as crystal structure, particle size, morphology, surface area and defect chemistry [51]. These properties are critically dependent on the chosen synthesis methodology. A diverse array of synthesis techniques has been explored to fabricate $CuMoO_4$ materials with tailored characteristics suitable for photocatalytic applications. This review section comprehensively discusses various synthesis routes reported for $CuMoO_4$-based materials, including hydrothermal [21], co-precipitation [20], thermal-decomposition to precipitation [24] and solid-state high-temperature [60]. The choice of synthesis technique is guided by the desired characteristics and intended applications of the $CuMoO_4$ material.

4.1 Hydrothermal Method

The hydrothermal method involves chemical reactions of substances in a sealed, heated aqueous solution or other solvents, above ambient temperature and pressure [61]. This technique

Copyright © 2026, ISSN 1978-2993

facilitates the dissolution of precursors, promotes nucleation and allows for the controlled growth of crystalline materials, often with unique morphologies [62,63].

A sea-urchin hollow $CuMoO_4$-$CoMoO_4$ hybrid microsphere were synthesized via a template-free hydrothermal approach [21]. The synthesis utilized 1 mmol of $CuCl_2{\cdot}2H_2O$, 1 mmol of $CoCl_2{\cdot}6H_2O$, and 4 mmol of $Na_2MoO_4{\cdot}2H_2O$ as precursors, dissolved in 30 ml of distilled water. The mixture was stirred for 30 min, then transferred to a 50 mL Teflon-lined stainless-steel autoclave and heated at 180 °C for 12 hours. Post-synthesis, the precipitate was collected, washed with distilled water and absolute ethanol, dried in a vacuum oven at 60 °C for 12 hours and finally calcined in air at 500 °C for 4 hours. The resulting materials exhibited a sea-urchin like hollow microsphere morphology with numerous nanorods on the surface.

It was found that hydrothermal synthesis of $CuMoO_4$ is optimized at the heating of 180 °C for 10 hours (Figure 7 (b)) [7]. Below 150 °C the reaction stops at $Cu_3Mo_2O_9$, which shows weak XRD peaks and hardly breaks down RhB (Figure 7 (a)). Above 200 °C, the crystals stop getting better and start to grow too big, so activity flattens out. For the photocatalytic degradation of RhB or 1H-benzotriazole, the optimal hydrothermal conditions were found to be at a temperature of 180 °C and a reaction time of 10 hours, corresponding to the high purity and highly

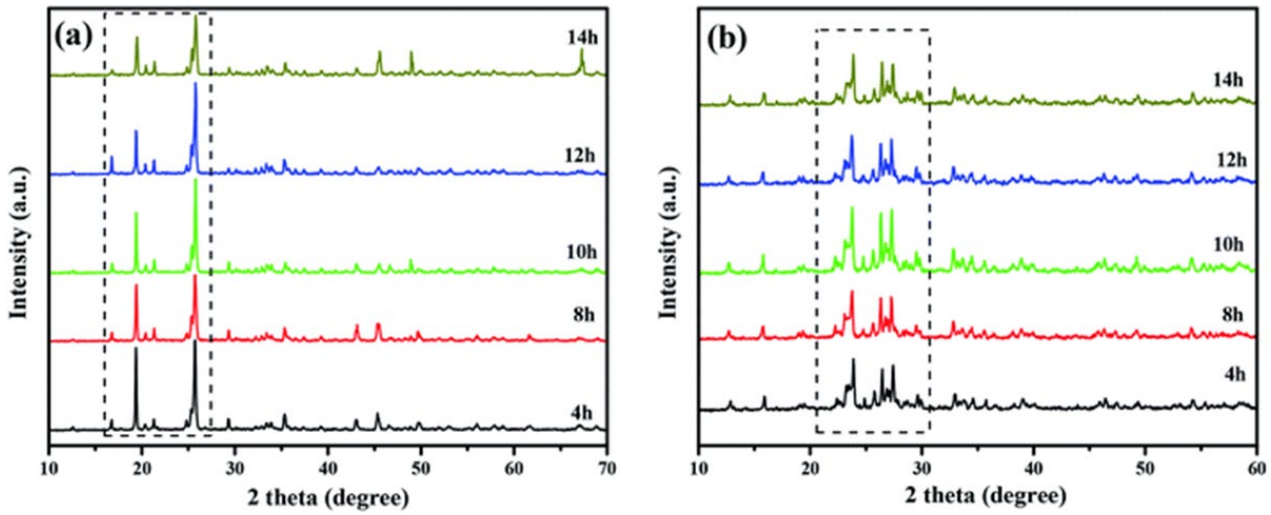

Figure 7. X-ray Diffraction (XRD) patterns tracking the crystallinity of $CuMoO_4$ with a) the amorphous precursor state and b) the evolution of crystalline phases at 180 °C over different hydrothermal durations (4-14 hours), identifying 10 hours as the optimal duration for high-purity phase formation [7].

Table 1. Summary of reported modification strategies for $CuMoO_4$-based photocatalysts, detailing synthesis methods, target pollutants, light sources, and degradation efficiencies. (N.S.: Not Specified.)

$CuMoO_4$-based photocatalyst	Synthesis method reported	Modification / engineering strategy	Pollutant(s) tested	Light source & power	Initial pollutant conc.	Catalyst loading ($g.L^{-1}$)	Degradation efficiency (%)	Time (min)	Ref.
ZnO/$CuMoO_4$ composite	Two-phase bio-interface (BVLE)	ZnO heterojunction	MG	Visible light, wattage not reported	5×10^{-6} M	N.S.	93.4	120	[51]
$CuMAP_2$ ($CuMoO_4$-doped $AlPO_4$)	Solid-solution co-precipitation	$CuMoO_4$ doped into $AlPO_4$	2-NA/4-NA	UV-visible lamp (power not given)	N.S.	0.15	100	8	[32]
$CuMoO_4$@g-C_3N_4 (CMC)	One-pot solvothermal	Z-scheme heterojunction	RhB/ Ciprofloxacin	Visible light, wattage not reported	N.S.	N.S.	98 / 97	35 / 60	[47]
ZnO/$CuMoO_4$ (hydro-microwave)	Hydrothermal + microwave	ZnO heterojunction	MB/RhB	UV lamp, wattage not reported	N.S.	0.02	92 / 84	70	[20]
$CuMoO_4$	Solid-state calcination 550 °C	Doping into $Bi_2Ti_4O_{11}$ alloy	Thymol blue	UV (lamp details not given)	3 ppm	3	50 % (T_{50})	244	[81]

Copyright © 2026, ISSN 1978-2993

crystalline $CuMoO_4$ whose exposed facets drive efficient visible-light catalysis.

In this study, the band gap of the $CuMoO_4$ synthesized under these conditions was estimated to be 1.97 eV and it was characterized as an indirect band gap semiconductor [7]. The study also acknowledged the existence of six known polymorphs of $CuMoO_4$, including the low-temperature α-$CuMoO_4$ and high-temperature ß-$CuMoO_4$, with the room-temperature triclinic (alpha) polymorph [7] being the focus of this investigation. A thermal analysis in Figure 8 indicated a phase transition around 570 °C.

These findings highlight that hydrothermal temperature is a crucial parameter for tailoring not only the crystallinity but also potentially the polymorphic phase of $CuMoO_4$. Different polymorphs can possess distinct electronic structures and surface characteristics, which would directly impact their photocatalytic activity.

4.2 Co-precipitation Method

Direct chemical precipitation is a widely used method for synthesizing inorganic materials, involving the formation of a solid product from a solution phase [64]. This occurs when precursor solutions containing copper and molybdate ions are mixed, leading to a reaction that yields an insoluble copper molybdate compound. Co-precipitation refers to the simultaneous precipitation of both copper and molybdate species. Variations of this method include surfactant-free or surfactant-assisted approaches, with subsequent steps typically involving washing, drying and often calcination to obtain the final material.

$CuMoO_4$ nanoparticles was also prepared through a co-precipitation method as a component for $CuMoO_4$/ZnO nanocomposites [20]. The precursors used were 3 M $CuSO_4$ and sodium dodecyl sulfate (SDS) as a surfactant, dissolved in deionized water and an aqueous solution of $(NH_4)_6Mo_7O_{24}·H_2O$. The molybdate-based solution was added dropwise to the copper-based solution and the mixture was heated to 65 °C for 2 hours. The greenish precipitate obtained was washed and dried in a vacuum at 60 °C. The average particle size of these $CuMoO_4$ nanoparticles was reported to be 190 nm and XRD confirmed the $CuMoO_4$ phase (JCPDS: 85-1530) [65]. Notably, FTIR analysis detected the presence of C-C bonds from unwashed SDS on the $CuMoO_4$ material. The resulting CuMoO4/ZnO nanocomposite demonstrated photocatalytic activity, degrading 92 % of MB and 84 % of RhB under UV irradiation after 70 min. Pure $CuMoO_4$ synthesized by this co-precipitation method showed 66 % degradation of MB and 59 % degradation of RhB under similar conditions.

While the ZnO/$CuMoO_4$ system demonstrates the efficacy of co-precipitation in forming effective heterojunctions, the versatility of this synthesis method is further evidenced by its successful application in other composite systems. For instance, recent studies on Ag-doped $CuMoO_4$ synthesized via co-precipitation have shown that this method allows for the precise incorporation of noble metal dopants into the lattice structure without inducing phase segregation. The co-precipitation route facilitates a uniform distribution of Ag nanoparticles (ranging from 60-120 nm), which act as electron sinks. This structural integration, achieved specifically through the controlled supersaturation inherent to co-precipitation, resulted in a MB degradation efficiency of nearly 99 % under visible light, significantly higher than that of pure $CuMoO_4$. The ability of this method to maintain stoichiometry at low temperatures prevents the agglomeration often seen in solid-state routes, thereby preserving the active surface sites required for dye adsorption [66,67].

Furthermore, the co-precipitation technique has proven vital in constructing g-C_3N_4/$CuMoO_4$ composites, where it addresses the common challenge of poor interfacial contact between the organic nitride nanosheets and the inorganic molybdate. Unlike physical mixing, in-situ co-precipitation allows $CuMoO_4$ nuclei to grow directly onto the g-C_3N_4 framework. This intimate contact, fostered by the gradual precipitation process, establishes a robust Z-scheme heterojunction that promotes efficient charge separation. Comparative data indicates that such co-precipitated g-C_3N_4/$CuMoO_4$ hybrids achieve degradation rates for cationic dyes (like MB) that are 1.3 to 1.5 times faster than their physically mixed counterparts [68,69]. Thus, the co-

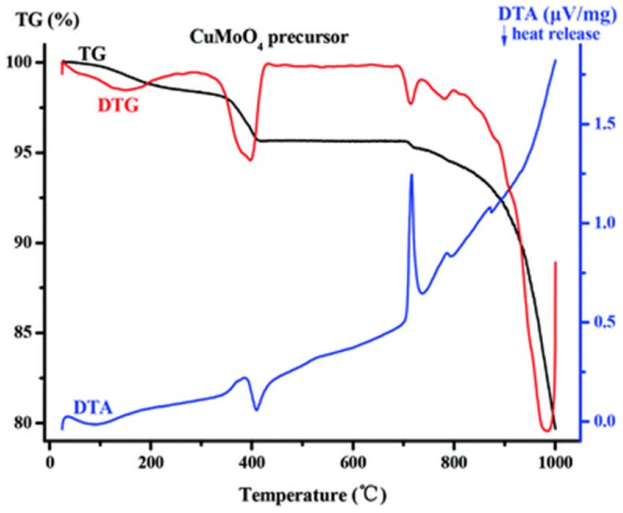

Figure 8. Thermal analysis (TG/DTA) of the $CuMoO_4$ precursor. The curves indicate weight loss events and heat flow changes, revealing a distinct phase transition and crystallization event occurring at approximately 570 °C. [7].

Copyright © 2026, ISSN 1978-2993

precipitation method is not merely a fabrication route but a critical strategy for engineering the interface quality essential for high-performance photocatalysis.

4.3 Thermal-decomposition Method

This category encompasses synthesis strategies where thermal decomposition is a key step, either occurring before or after a precipitation event, to yield the final $CuMoO_4$ material. One approach involves thermally decomposing initial precursors to generate reactive species that subsequently precipitate as $CuMoO_4$ nanoparticles (NPs), a synthesis route reported via the sequential thermal decomposition to precipitation method [24], as shown in Figure 9. Different copper concentrations from 0.1 M, 0.2 M, and 0.3 M were used, which affected the band gap of the resulting $CuMoO_4$ (1.97 eV, 1.86 eV, and 1.44 eV, respectively). The 0.3 M $CuMoO_4$ NPs exhibited superior photocatalytic efficiency for MB degradation, attributed to a low electron-hole recombination rate.

A more commonly encountered route precipitates an intermediate precursor that is then thermally decomposed (calcined or sintered) to yield the final $CuMoO_4$ material. The strategy of precipitating an intermediate followed by thermal decomposition is a prevalent and effective means of producing crystalline $CuMoO_4$-based materials, often allowing for good morphological control [24]. The thermal decomposition step is crucial for phase formation, enhancement of crystallinity and removal of volatile components from the precipitated precursor [70,71]. This two-step approach can offer superior control over the final properties of the synthesized materials, compared to direct high-temperature methods, as the characteristics of the precursor such as size and shape can be tailored first, often influencing the morphology of final product. The alternative thermal decomposition-precipitation sequence [24] is less conventional for molybdates and requires further clarification of its specific mechanism and experimental details.

4.4 Solid-State High-Temperature Reaction

The solid-state reaction typically involves intimately mixing solid precursors (often metal oxides or salts) in stoichiometric proportions, followed by one or more high-temperature calcination or sintering steps [72]. These elevated temperatures facilitate solid-state diffusion and chemical reaction between the components, leading to the formation of the desired compound.

Polycrystalline α-$CuMoO_4$ photocatalysts were synthesized by a conventional solid-state reaction using high-purity CuO and MoO_3 as precursors [60]. These precursors were mixed stoichiometrically and meticulously ground in an agate mortar. The mixture was then sealed in platinum crucibles and subjected to a first heat treatment at 500 °C for 16 hours. After this step,

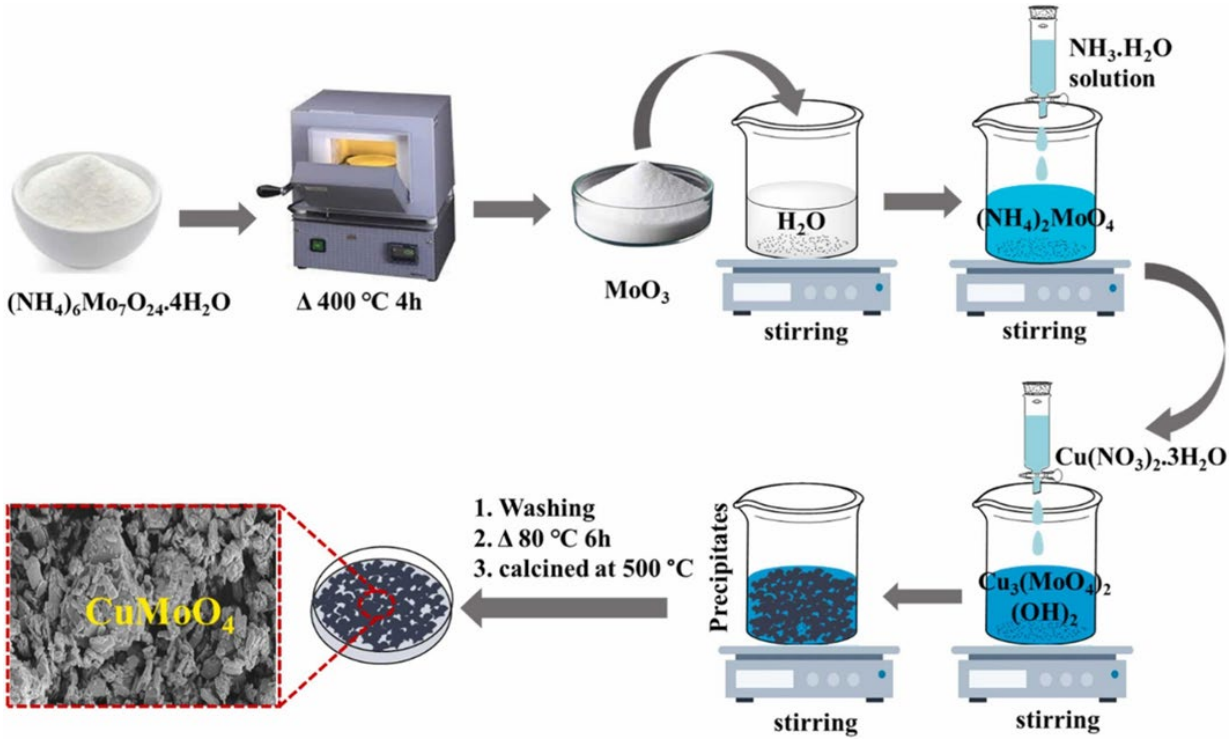

Figure 9. Schematic workflow of the thermal-decomposition synthesis route for $CuMoO_4$ nanoparticles. The process involves the initial reaction of molybdate and copper precursors to form an intermediate precipitate, followed by washing, drying and calcination at 500 °C to achieve the final crystalline product [24].

Copyright © 2026, ISSN 1978-2993

the samples were ground again and then underwent a second heat treatment at 650 °C for 14 hours to ensure homogeneity and complete reaction for α-$CuMoO_4$ formation. Finally, the reaction products were cooled at a rate of 393 K/h to room temperature. XRD analysis as shown in Figure 10 confirmed the formation of α-$CuMoO_4$, which crystallized in the triclinic system with the $P\bar{1}$ space group. A minor secondary phase of approximately 2 % MoO_3 was also detected.

Solid-state synthesis is effective for producing highly crystalline and thermodynamically stable phases of $CuMoO_4$, such as the α-$CuMoO_4$. However, a general characteristic of this method is the production of materials with relatively larger particle sizes and consequently lower specific surface areas compared to those typically obtained via wet-chemical routes [73]. This can be a disadvantage for photocatalytic applications where a high surface area is often crucial for providing sufficient active sites [74]. The main advantages of solid-state reactions lie in their simplicity for bulk powder synthesis and their ability to achieve thermodynamic equilibrium phases [75].

This section reviews a range of synthesis methodologies for $CuMoO_4$-based photocatalysts, encompassing hydrothermal techniques, co-precipitation, thermal decomposition involving precipitation and solid-state high-temperature reactions. Each method presents distinct advantages and challenges in terms of controlling crucial physicochemical properties that dictate photocatalytic efficacy. A notable observation across several wet-chemical methods (precipitation, hydrothermal routes involving precursor formation and methods leading to intermediate compounds) is the frequent and often critical role of post-synthesis calcination or

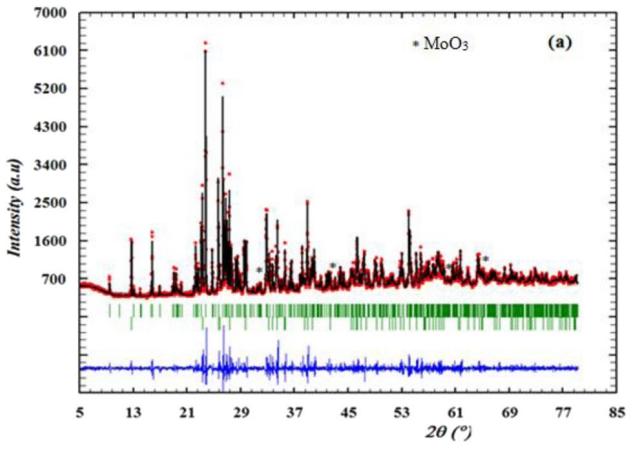

Figure 10. Observed (red dots) and calculated (black line) X-ray diffraction patterns from the Rietveld refinement of solid-state synthesized α-$CuMoO_4$. The analysis confirms the sample crystallizes in the triclinic system (space group P1) with a minor MoO_3 impurity phase [60].

sintering [76]. This thermal treatment step is essential for achieving the desired crystalline phase, removing volatile impurities or solvent residues and ultimately activating the photocatalytic potential of the $CuMoO_4$ material. The temperature and duration of calcination are themselves critical parameters influencing the final properties [77,78].

The selection of an appropriate synthesis strategy is of importance it directly affects the characteristics of the material and consequently, its performance in the photocatalytic degradation of persistent organic pollutants. Understanding the relationship between synthesis parameters, post-synthesis treatments and the resultant structural and electronic properties is vital for the rational design and reproducible fabrication of highly efficient $CuMoO_4$-based photocatalysts. Future research should continue to focus on establishing clearer structure-property-activity relationships that are directly linked to specific and well-documented synthesis protocols of $CuMoO_4$-based materials. The following Table 2 summarizes the key details from the discussed synthesis methods for $CuMoO_4$-based materials as reported in the provided literature.

5. Stability, Recyclability and Practical Application

While the initial photocatalytic activity of $CuMoO_4$ is promising, its practical industrial application hinges on long-term stability and recyclability. A primary concern for copper-based photocatalysts is the potential leaching of Cu^{2+} ions into the treated effluent, which can lead to secondary pollution. Although $CuMoO_4$ is generally stable at neutral pH, acidic conditions (pH < 4) can accelerate the dissolution of the copper sub-lattice [79]. Most studies evaluate recyclability over 4 to 5 consecutive cycles, typically reporting a minor efficiency loss of < 5%, which is often attributed to the physical loss of catalyst powder during recovery rather than chemical deactivation [80]. However, rigorous quantification of dissolved copper in the final effluent is frequently omitted in the literature. Recent work [79] highlighted that while Mo-based phases can suffer from leaching, optimizing the synthesis method (e.g., sol-gel vs. co-precipitation) and incorporating carbonaceous supports (like graphene oxide or biochar) can significantly enhance chemical stability by shielding the active sites from photocorrosion [74]. Furthermore, a significant gap remains between laboratory results and real-world application. The vast majority of current research utilizes simulated wastewater containing single model dyes such as MB or RhB in deionized water. In contrast, real industrial effluents contain complex mixtures of inorganic ions (Cl-, SO_4^{2-}, CO_3^{2-}), natural organic

Copyright © 2026, ISSN 1978-2993

matter and varying pH levels, all of which can act as radical scavengers and deactivate surface active sites. Future research must prioritize testing in real wastewater matrices and exploring scalable reactor designs, such as immobilized catalyst beds or continuous flow systems, to validate the techno-economic viability of $CuMoO_4$ technologies.

6. Conclusion and Outlook

Photocatalytic degradation of refractory organics using $CuMoO_4$-based materials has progressed rapidly over the past six years, moving from simple hydrothermal powders to sophisticated, multi-component architectures under visible irradiation. A comparative analysis

Table 2. Comparative overview of synthesis methodologies for $CuMoO_4$-based materials. The table lists precursor materials, reaction conditions and resulting morphological properties for hydrothermal, co-precipitation, thermal-decomposition and solid-state routes.

Synthesis Method	Specific $CuMoO_4$ Material / Phase	Copper Precursor (s)	Molybdenum Precursor (s)	Solvent (s) / Medium	Key Reaction Parameters	Post-Synthesis Treatment	Morphology / Size	Ref.
Conventional Hydrothermal	$CuMoO_4$ –$CoMoO_4$ hybrid microspheres	$CuCl_2{\cdot}2H_2O$ (1 mmol)	$Na_2MoO_4{\cdot}2H_2O$ (4 mmol)	Distilled water (30 mL)	180 °C, 12 hours (Co-precursor: $CoCl_2{\cdot}6H_2O$, 1 mmol)	Washed, dried (60 °C, 12 h, vacuum), calcined (500 °C, 4 hours, air)	Sea-urchin-like hollow microspheres with nanorods on surface	[21]
Temperature-Controlled "in-situ" Hydrothermal	$CuMoO_4$	N.S.	N.S.	N.S.	Optimal: 180 °C, 10 hours. Disparate hydrothermal temperatures lead to different samples.	N.S.	N.S.	[7]
Direct Chemical Precipitation (Surfactant-Free)	$CuMoO_4$ nanoparticles	Cupric acetate monohydrate $[(CH_3COO)_2Cu{\cdot}H_2O]$	Sodium molybdate $[Na_2MoO_4]$	Double-distilled water	Room temperature, dropwise addition, continuous stirring.	Washed (water, ethanol), air-dried (2 days), calcined (600 °C, 5 hours)	Rock-like structure, nanometer range nanoparticles	[76]
Direct Chemical Precipitation (Co-precipitation with Surfactant)	$CuMoO_4$ nanoparticles	3M $CuSO_4$	$(NH_4)_6Mo_7O_{24}{\cdot}H_2O$ (aq.)	Deionized water	Heated to 65 °C for 2 hours. SDS as surfactant. Dropwise addition.	Washed, dried (vacuum, 60 °C)	Average particle size 190 nm	[74]
Thermal-Decomposition	$CuMoO_4$ NPs	Cu precursor (0.1, 0.2, 0.3 M concentrations mentioned)	Mo precursor (not specified)	N.S.	Details of thermal decomposition and precipitation steps not provided.	N.S.	Nanoparticles	[24]
Solid-State High-Temperature Reaction	α-$CuMoO_4$ powder	CuO (≥99%)	MoO_3 (≥99%)	Solid state	Mixed, ground. 1st heat: 773 K (500 °C), 16 hours. Ground. 2nd heat: 923 K (650 °C), 14 hours. Cooled 393 K/h.	None	Polycrystalline powder (particle size not specified)	[60]
Sonochemical	$CuMoO_4$ nanoparticles	$Cu(NO_3)_2{\cdot}6H_2O$	$(NH_4)_6Mo_7O_{24}{\cdot}4H_2O$	Distilled water (30 mL)	Ultrasonic irradiation (probe, 20 kHz, 50 W)	Filtered, washed with water & ethanol; dried at 60 °C for 1 hour	Spherical nanoparticles, 50–55 nm	[27]

Copyright © 2026, ISSN 1978-2993

of > 60 studies reveal that morphology alone typically yields less than a twofold increase in activity. It is recommended that combining shape control with heterojunction formation or defect engineering can boost rate constants and quantum yields by nearly ten times. Another important finding is that band-structure adjustments via such as creating oxygen vacancies or co-doping with aluminum or phosphorus would narrow the band gap, introduce donor states and slow electron-hole recombination, enhancing sunlight utilization without sacrificing redox power. Another major finding from this review is the incorporation of plasmonic or single-atom co-catalysts which accelerates interfacial reactions. This approach however poses cost and stability challenges, from nanoparticle aggregation to copper leaching, which drives the search for lower-cost, more durable alternatives like copper-rich defect phases or carbon-based additives. To date, hierarchical heterojunctions deliver the best balance of broad light absorption and strong redox capability, achieving over 95 % removal of antibiotics and dyes in 30 to 70 min under natural or simulated sunlight.

Despite these advances, there is an issue posed by the mechanistic precision. In-situ spectroscopies (EPR, XPS, ATR-FTIR) and time-resolved photoluminescence are ideal, coupled with density-functional theory (DFT) to map charge-carrier dynamics, identify true active sites and predict optimal compositional spaces. Furthermore, bridging the gap between laboratory efficiency and industrial viability will require a shift from simple dye-degradation studies to rigorous pilot-scale evaluations involving complex wastewater matrices. Addressing these combined fundamental and engineering challenges will pave the way for robust, low-cost $CuMoO_4$ photocatalysts capable of broad environmental application and aligning with sustainable-development goals (SDG).

Acknowledgment

The authors express their gratitude to the internal grant of UMPSA (RDU230393), Sustainable Research Collaboration Grant UMPSA- International Islamic University Malaysia (IIUM) (RDU223223) and financial support from Tabung Persidangan Dalam Negara (TPDN) via Jabatan Penyelidikan dan Inovasi of UMPSA.

CRedit Author Statement

Author Contributions: H. Abdullah: funding acquisition, investigation and formal analysis; R. Jusoh: investigation; W. Safie: investigation, formal analysis; R. R. Nasaruddin: formal analysis; M. R. Khan: investigation; M. N. Arifin: conceptualization, project administration, & editing. All authors have read and agreed to the published version of the manuscript.

References

[1] Arifin, M.N., Jusoh, R., Abdullah, H., Ainirazali, N., Setiabudi, H.D. (2023). Recent advances in advanced oxidation processes (AOPs) for the treatment of nitro- and alkyl-phenolic compounds. *Environmental Research*, 229, 115936. DOI: 10.1016/j.envres.2023.115936.

[2] Gmurek, M., Olak-Kucharczyk, M., Ledakowicz, S. (2017). Photochemical decomposition of endocrine disrupting compounds – A review. *Chemical Engineering Journal*, 310, 437–456. DOI: 10.1016/j.cej.2016.05.014.

[3] Young, B.J., López, G.C., Cristos, D.S., Crespo, D.C., Somoza, G.M., Carriquiriborde, P. (2017). Intersex and liver alterations induced by long-term sublethal exposure to 17α-ethinylestradiol in adult male Cnesterodon decemmaculatus (Pisces: Poeciliidae). *Environmental Toxicology and Chemistry*, 36(7), 1738–1745. DOI: 10.1002/etc.3547.

[4] Foster, D., Brown, K. (2018). Dose Duration Effects of 17-α Ethynylestradiol in Zebrafish Toxicology. In *Recent Advances in Zebrafish Researches*, Edited by Yusuf Bozkurt. DOI: 10.5772/intechopen.74639.

[5] Kumar, P., Boukherroub, R., Shankar, K. (2018). Sunlight-driven water-splitting using two-dimensional carbon based semiconductors. *J. Mater. Chem. A*, 6(27), 12876–12931. DOI: 10.1039/C8TA02061B.

[6] Rengifo-Herrera, J.A., Osorio-Vargas, P., Pulgarin, C. (2022). A critical review on N-modified TiO2 limits to treat chemical and biological contaminants in water. Evidence that enhanced visible light absorption does not lead to higher degradation rates under whole solar light. *Journal of Hazardous Materials*, 425, 127979. DOI: 10.1016/j.jhazmat.2021.127979.

[7] Tan, W., Luan, J. (2020). Investigation into the synthesis conditions of CuMoO4 by an in situ method and its photocatalytic properties under visible light irradiation. *RSC Advances*, 10(16), 9745–9759. DOI: 10.1039/D0RA00496K.

[8] Kuku, M., Althahban, S., Arishi, M. (2024). Diffusion-dominated redox performance of hydrated copper molybdate for high-performance energy storage. *Inorg. Chem. Front.*, 11(23), 8258–8271. DOI: 10.1039/D4QI02229G.

Copyright © 2026, ISSN 1978-2993

[9] Gurusamy, L., Karuppasamy, L., Anandan, S., Liu, C.-H., Wu, J.J. (2024). Recent advances on metal molybdate-based electrode materials for supercapacitor application. *Journal of Energy Storage*, 79, 110122. DOI: 10.1016/j.est.2023.110122.

[10] Abd Aziz, A., Khatun, F., Monir, M., Ching, S., Leong, K. (2021). TiO2 : A Semiconductor Photocatalyst. In *Titanium Dioxide - Advances and Applications*. Edited by: Hafiz Muhammad Ali pp. 1–16. DOI: 10.5772/intechopen.99256.

[11] Dong, H., Chen, Y.-C., Feldmann, C. (2015). Polyol synthesis of nanoparticles: status and options regarding metals, oxides, chalcogenides, and non-metal elements. *Green Chem*., 17(8), 4107–4132. DOI: 10.1039/C5GC00943J.

[12] Kamarasu, L., Sathiyamoorthi, E., Nannapaneni, S.S., Arunachalam, S., Arunpandian, M., Lee, J., Arumugam, P., Katari, N.K. (2023). Enhanced photocatalytic performance of pebble stone like CuMoO4 photocatalyst for the degradation of organic pollutant. *Physica B: Condensed Matter*., 650, 414544. DOI: 10.1016/j.physb.2022.414544.

[13] Wu, Y., Wang, H. (2023). Construction of CuMoO4/MnO2/tourmaline composite for efficient organic wastewater decontamination via photo-Fenton-like processes. *Journal of Environmental Chemical Engineering*, 11(6), 111190. DOI: 10.1016/j.jece.2023.111190.

[14] Gaur, N., Dutta, D., Singh, A., Dubey, R., Kamboj, D. (2022). Recent advances in the elimination of persistent organic pollutants by photocatalysis. *Frontiers in Environmental Science*, 10, 22076. DOI: 10.3389/fenvs.2022.872514.

[15] Toe, C.Y., Zheng, Z., Wu, H., Scott, J., Amal, R., Ng, Y.H. (2018). Photocorrosion of Cuprous Oxide in Hydrogen Production: Rationalising Self-Oxidation or Self-Reduction. *Angewandte Chemie International Edition*, 57(41), 13613–13617. DOI: 10.1002/anie.201807647.

[16] Vinay, G., Ashwini, G.R., Shivaraj, Y. (2025). Construction of Y-CuMoO4 heterojunction nanocomposites for toxic methylene blue dye removal and electrocatalytic sensing of 3-chlorophenol. *Analytical Methods*. DOI: 10.1039/D5AY01483B

[17] Belousov, A.S., Parkhacheva, A.A., Suleimanov, E. V., Fukina, D.G., Koryagin, A.V., Shafiq, I., Krasheninnikova, O.V., Kuzmichev, V.V. (2023). Doping vs. heterojunction: A comparative study of the approaches for improving the photocatalytic activity of flower-like Bi2WO6 for water treatment with domestic LED light. *Catalysis Communications*, 180, 106705. DOI: 10.1016/j.catcom.2023.106705.

[18] Gai, D., Li, X., Lin, H., Yuan, R., Long, J., Lin, Q. (2025). Synthesis of the Type II Heterojunction of CeO2/CuMoO4 for Improving the Antibacterial Activity of Photocatalysis. *ACS Applied Bio Materials*, 8(8), 7126–7138. DOI: 10.1021/ACSABM.5C00885.

[19] Li, Q., Jin, F., Yuan, M., Xu, C., Jin, Z. (2026). Carbon coating-induced electron-thermal synergistic modulation for enhanced photocatalytic hydrogen evolution over CdS/CuMoO4 heterojunctions. *Applied Catalysis B: Environment and Energy*, 384, 126168. DOI: 10.1016/j.apcatb.2025.126168.

[20] Tanjung, F., Syah, B.R., Altajer, A., Abdul-Rasheed, O., Aljeboree, A., Abd Alrazzak, N., Alkaim, A. (2021). CuMoO4/ZnO Nanocomposites: Novel Synthesis, Characterization, and Photocatalytic Performance. *Journal of Nanostructures*. 11(1), 69–80. DOI: 10.22052/JNS.2021.01.009.

[21] Feng, Y., Shao, Y., Chen, X., Zhang, Y., Liu, Q., He, M., Li, H. (2021). Sea-Urchin-like Hollow CuMoO4–CoMoO4 Hybrid Microspheres, a Noble-Metal-like Robust Catalyst for the Fast Hydrogen Production from Ammonia Borane. *ACS Applied Energy Materials*, 4(1), 633–642. DOI: 10.1021/acsaem.0c02521.

[22] Nassau, K., Abrahams, S.C. (1968). The growth and properties of single crystal cupric molybdate. Journal of Crystal Growth, 2(3), 136–140. DOI: 10.1016/0022-0248(68)90076-6.

[23] Abrahams, S.C., Bernstein, J.L., Jamieson, P.B. (1968). Crystal Structure of the Transition - Metal Molybdates and Tungstates. IV. Paramagnetic CuMoO4. *The Journal of Chemical Physics*, 48(6), 2619 – 2629. DOI: 10.1063/1.1669492.

[24] Alabada, R., Ayub, A., Ajaj, Y., Bhat, S., Alshammari, R., Abduldayeva, A., Mallhi, A., Ahmad, Z., Mohamed, R. (2024). A new approach to the synthesis of CuMoO4 nanoparticles with mechanistic insight into the sunlight-assisted degradation of textile pollutants and antibacterial activity evaluation. *Journal of Alloys and Compounds*, 977, 1–14. DOI: 10.1016/j.jallcom.2023.173400.

[25] Roy, N., Sohn, Y., Pradhan, D. (2013). Synergy of Low-Energy {101} and High-Energy {001} TiO2 Crystal Facets for Enhanced Photocatalysis. *ACS Nano*, 7(3), 2532–2540. DOI: 10.1021/nn305877v.

[26] Li, J., Gong, Y., Li, J., Fan, L. (2023). Hydrothermal treatment improves xanthine oxidase inhibitory activity and affects the polyphenol profile of Flos Sophorae Immaturus. *Journal of the Science of Food and Agriculture*, 103(3), 1205–1215. DOI: 10.1002/jsfa.12215.

[27] Sadeghi, M. (2016). Investigation of the structural, optical and magnetic properties of CuMoO4 nanoparticles synthesized through a sonochemical method. *Journal of Materials Science: Materials in Electronics*, 27. DOI: 10.1007/s10854-016-4494-5.

[28] Dummer, N., Sodiq-Ajala, Z., Morgan, D., Davies, T. (2022). Investigating the preparation of Cu3Mo2O9 as a photocatalyst. *Catalysis Communications*, 163, 106414. DOI: 10.1016/j.catcom.2022.106414.

Copyright © 2026, ISSN 1978-2993

[29] Liu, Z., Hadi, M.A., Aljuboory, D.S., Ali, F.A., Jawad, M.A., AL-Alwany, A., Hadrawi, S.K., Mundher, T., Riadi, Y., Amer, R.F., Fakhri, A. (2022). High efficiency of Ag0 decorated Cu2MoO4 nanoparticles for heterogeneous photocatalytic activation, bactericidal system, and detection of glucose from blood sample. *Journal of Photochemistry and Photobiology B: Biology*, 236, 112571. DOI: 10.1016/j.jphotobiol.2022.112571.

[30] Yu, L., Li, N. (2019). Noble Metal Nanoparticles-Based Colorimetric Biosensor for Visual Quantification: A Mini Review. *Chemosensors*, 7(4). DOI: 10.3390/chemosensors7040053.

[31] Liu, Y., Wang, W., Xu, X., Marcel Veder, J.-P., Shao, Z. (2019). Recent advances in anion-doped metal oxides for catalytic applications. *J. Mater. Chem. A*, 7(13), 7280–7300. DOI: 10.1039/C8TA09913H.

[32] Ghorai, T.K., Chakraborty, S., Satpute, N., Mehmood, S., Kumar, N., Sahu, S.K., Ghosh, M.K. (2023). A new copper molybdate-doped aluminium phosphate nanocomposite heterostructure for photoreduction of aqueous 2-NA and 4-NA. *Mater. Adv.*, 4(11), 2487–2493. DOI: 10.1039/D3MA00152K.

[33] Živković, A., Roldan, A., Leeuw, N. (2019). Tuning the electronic band gap of Cu2O via transition metal doping for improved photovoltaic applications. *Physical Review Materials*, 3. DOI: 10.1103/PhysRevMaterials.3.115202.

[34] Yao, C., Feng, H., Weng, S., Li, J., Huo, Y.-F., Yan, W., Dong, R., Yang, L. (2025). Cu2O1–x-Superlattices Induced Oxygen Vacancy for Localized Surface Plasmon Resonance. *Nano Letters*, 25(2), 922–930. DOI: 10.1021/acs.nanolett.4c06330.

[35] Yang, Y., Shi, Z., Zang, H., Ma, X., Fan, D., Bai, J., Zhang, F., Jiang, K., Lv, S., Li, S., Sun, X., Li, D. (2024). How do the oxygen vacancies affect the photoexcited carriers dynamics in β-Ga2O3? . *Materials Today Physics*, 40, 101328. DOI: 10.1016/j.mtphys.2024.101328.

[36] Prakash, A., Mahesha, M.G. (2023). Harnessing the tunability of intrinsic defects in isovalent Zn doped spray deposited CuO thin films. *Materials Chemistry and Physics*, 309, 128443. DOI: 10.1016/j.matchemphys.2023.128443.

[37] Qiu, Q., Zhao, L., Li, S., Wang, D., Xu, L., Lin, Y., Xie, T. (2016). Suppress the Charge Recombination in Quantum Dot Sensitized Solar Cells by Construct the Al–treated TiO2/TiO2 NRAs Heterojunctions. *ChemistrySelect*, 1(18), 5936–5943. DOI: 10.1002/slct.201600953.

[38] Wang, J., Wang, S. (2022). A critical review on graphitic carbon nitride (g-C3N4)-based materials: Preparation, modification and environmental application. *Coordination Chemistry Reviews*, 453, 214338. DOI: 10.1016/j.ccr.2021.214338.

[39] Xu, Q., Zhang, L., Cheng, B., Fan, J., Yu, J. (2020). S-Scheme Heterojunction Photocatalyst. *Chem*, 6(7), 1543–1559. DOI: 10.1016/j.chempr.2020.06.010.

[40] Tong, X., Wei, Q., Zhan, X., Zhang, G., Sun, S. (2017). The New Graphene Family Materials: Synthesis and Applications in Oxygen Reduction Reaction. *Catalysts*, 7(1) DOI: 10.3390/catal7010001.

[41] Singh, G., Sai Bhargava, V., Sharma, M. (2018). Synthesis of graphene oxide–copper molybdate (GO-CuM) nanocomposites for photocatalytic application. *AIP Conference Proceedings*, 1961(1), 030004. DOI: 10.1063/1.5035206.

[42] Khan, M.R., Abdullah, H., Safiei, W., Handani, Z.B., Nasaruddin, R.R., Arifin, M.N. (2025). Science mapping of TiO2 modification strategies for wastewater treatment: Current and future trends. *Journal of Physics: Conference Series*, 3003(1), 012038. DOI: 10.1088/1742-6596/3003/1/012038.

[43] Phan, D.-T., Chung, G.-S. (2013). P–n junction characteristics of graphene oxide and reduced graphene oxide on n-type Si(111). *Journal of Physics and Chemistry of Solids*, 74(11), 1509–1514. DOI: 10.1016/j.jpcs.2013.02.007.

[44] Zhang, X.-F., Xi, Q. (2011). A graphene sheet as an efficient electron acceptor and conductor for photoinduced charge separation. Carbon, 49, 3842–3850. DOI: 10.1016/j.carbon.2011.05.019.

[45] [45] Minitha, C.R., Lalitha, M., Jeyachandran, Y.L., Senthilkumar, L., Rajendra Kumar, R.T. (2017). Adsorption behaviour of reduced graphene oxide towards cationic and anionic dyes: Co-action of electrostatic and π – π interactions. *Materials Chemistry and Physics*, 194, 243–252. DOI: 10.1016/j.matchemphys.2017.03.048.

[46] Muhmood, T., Ahmad, I., Haider, Z., Haider, S.K., Shahzadi, N., Aftab, A., Ahmed, S., Ahmad, F. (2024). Graphene-like graphitic carbon nitride (g-C3N4) as a semiconductor photocatalyst: Properties, classification, and defects engineering approaches. *Materials Today Sustainability*, 25, 100633. DOI: 10.1016/j.mtsust.2023.100633.

[47] Kasirajan, P., Karunamoorthy, S., Velluchamy, M., Subramaniam, K., Park, C.M., Sundaram, G.B. (2023). Fabrication of copper molybdate nanoflower combined polymeric graphitic carbon nitride heterojunction for water depollution: Synergistic photocatalytic performance and mechanism insight. *Environmental Research*, 233, 116428. DOI: 10.1016/j.envres.2023.116428.

[48] Bhanderi, D., Lakhani, P., Modi, C.K. (2024). Graphitic carbon nitride (g-C3N4) as an emerging photocatalyst for sustainable environmental applications: a comprehensive review. *RSC Sustainability*, 2(2), 265–287. DOI: 10.1039/d3su00382e.

[49] Sultana, N., Priyadarshini, P., Parida, K. (2025). UiO-66-NH2 and its functional nanohybrids: unlocking photocatalytic potential for clean energy and environmental remediation. *Sustainable Energy Fuels*, 9, 3458-3494. DOI: 10.1039/D5SE00150A.

Copyright © 2026, ISSN 1978-2993

[50]. Qiu, Z., Li, Y., Long, X., Tian, H., Pu, Y., Lv, B., Wei, J., Dai, Q., Wang, W. (2024). Built-in electric field induced efficient interfacial charge separation via the intimate interface of CdS-based all-sulfide binary heterojunction for enhanced photoelectrochemical performance. *Journal of Alloys and Compounds*, 976, 173188. DOI: 10.1016/j.jallcom.2023.173188.

[51]. Kusumah, A.D., Yulizar, Y., Apriandanu, D.O.B., Surya, R.M. (2024). Fabrication of ZnO and ZnO/CuMoO4 for the improvement of photocatalytic performance. *Vacuum*, 222, 113034. DOI: 10.1016/j.vacuum.2024.113034.

[52]. Jafarova, V.N., Orudzhev, G.S. (2021). Structural and electronic properties of ZnO: A first-principles density-functional theory study within LDA(GGA) and LDA(GGA)+U methods. *Solid State Communications*, 325, 114166. DOI: 10.1016/j.ssc.2020.114166.

[53]. Che, L., Pan, J., Cai, K., Cong, Y., Lv, S.-W. (2023). The construction of p-n heterojunction for enhancing photocatalytic performance in environmental application: A review. *Separation and Purification Technology*, 315, 123708. DOI: 10.1016/j.seppur.2023.123708

[54]. Ghorai, T.K., Ghorai, T.K. (2011). Photocatalytic Degradation of 4-chlorophenol by CuMoO4-doped TiO2 Nanoparticles Synthesized by Chemical Route. *Open Journal of Physical Chemistry*, 1(2), 28–36. DOI: 10.4236/ojpc.2011.12005.

[55]. Meng, X., Hao, M., Shi, J., Cao, Z., He, W., Gao, Y., Liu, J., Li, Z. (2017). Novel CuO/Bi2WO6 heterojunction with enhanced visible light photoactivity. *Advanced Powder Technology*, 28(12), 3247–3256. DOI: 10.1016/j.apt.2017.09.036.

[56]. Kumar, A., Raizada, P., Khan, A.A.P., Nguyen, V.-H., Van Le, Q., Singh, A., Saini, V., Selvasembian, R., Huynh, T.-T., Singh, P. (2021). Phenolic compounds degradation: Insight into the role and evidence of oxygen vacancy defects engineering on nanomaterials. *Science of The Total Environment*, 800, 149410. DOI: 10.1016/j.scitotenv.2021.149410.

[57]. Hao, L., Huang, H., Zhang, Y., Ma, T. (2021). Oxygen Vacant Semiconductor Photocatalysts. *Advanced Functional Materials*, 31(25), 2100919. DOI: 10.1002/adfm.202100919.

[58]. Gan, J., Lu, X., Wu, J., Xie, S., Zhai, T., Yu, M., Zhang, Z., Mao, Y., Wang, S.C.I., Shen, Y., Tong, Y. (2013). Oxygen vacancies promoting photoelectrochemical performance of In2O3 nanocubes. *Scientific Reports*, 3(1), 1021. DOI: 10.1038/srep01021.

[59]. Liu, Y., Peng, Y., Naschitzki, M., Gewinner, S., Schöllkopf, W., Kuhlenbeck, H., Pentcheva, R., Roldan Cuenya, B. (2021). Surface oxygen Vacancies on Reduced Co3O4(100): Superoxide Formation and Ultra-Low-Temperature CO Oxidation. *Angewandte Chemie International Edition*, 60(30), 16514–16520. DOI: 10.1002/anie.202103359.

[60]. Chakchouk, N., Karoui, K., Drissi, N., Jomni, F., Ben Rhaiem, A. (2024). An investigation of structural, thermal, and electrical conductivity properties for understanding transport mechanisms of CuWO4 and α-CuMoO4 compounds. *RSC Advances*, 14(1), 46–58. DOI: 10.1039/D3RA07453F.

[61]. Feng, S., Xu, R. (2001). New Materials in Hydrothermal Synthesis. *Accounts of Chemical Research*, 34(3), 239–247. DOI: 10.1021/ar0000105.

[62]. Li, J., Wu, Q., Wu, J. (2015). Synthesis of Nanoparticles via Solvothermal and Hydrothermal Methods. In: Aliofkhazraei, M. (ed) *Handbook of Nanoparticles*. Cham: Springer International Publishing, pp. 1–28.DOI: 10.1007/978-3-319-13188-7_17-1.

[63]. Upadhyay, S., Varma, V., Pundhir, D. (2024). A Brief Study of Synthesis of Metallic Nanoparticles via Hydrothermal Process. DOI: 10.52458/9788197112492.nsp.2024.eb.ch-05.

[64]. Joe Pushba Shini, J., Joy Prabu, H., Felix Sahayaraj, A., Johnson, I., Thaninayagam, E., Gopi, R.R., Snowlin, V. (2024). Synthesis of hydroxyapatite (HAp) from eggshells via thermal decomposition method for the application of dye adsorption. *Journal of the Indian Chemical Society*, 101(10), 101321. DOI: 10.1016/j.jics.2024.101321.

[65]. Gil-García, R., Zichner, R., Díez-Gómez, V., Donnadieu, B., Madariaga, G., Insausti, M., Lezama, L., Vitoria, P., Pedrosa, M.R., García-Tojal, J. (2010). Polyoxometallate-thiosemicarbazone hybrid compounds. *European Journal of Inorganic Chemistry*, 2010(28), 4513–4525. DOI: 10.1002/ejic.201000484.

[66]. Blažeka, D., Radičić, R., Maletić, D., Živković, S., Momčilović, M., Krstulović, N. (2022). Enhancement of Methylene Blue Photodegradation Rate Using Laser Synthesized Ag-Doped ZnO Nanoparticles. *Nanomaterials*, 12(15), 2677. DOI: 10.3390/nano12152677/S1.

[67]. Baral, S.C., Saint, U.K., Sasmal, D., Lenka, S., Kalkal, A., Mekki, A., Pitchaimuthu, S., Sen, S. (2025). Interfacial Synergy in Ag-Doped CuO-AgCl-g-C3N4 Composites for Efficient Charge Separation and Low-power Methylene Blue Degradation *Journal of Inorganic and Organometallic Polymers and Materials*, 31, 258–271. DOI: 10.48550/arXiv.2512.04825.

[68]. Hanif, M.A., Akter, J., Kim, Y.S., Kim, H.G., Hahn, J.R., Kwac, L.K. (2022). Highly Efficient and Sustainable ZnO/CuO/g-C3N4 Photocatalyst for Wastewater Treatment under Visible Light through Heterojunction Development. *Catalysts*, 12(2), 151. DOI: 10.3390/catal12020151/S1.

[69]. Shi, W., Guo, F., Lin, X., Hong, Y. (Eds.). (2023). Development of g-C3N4-Based Photocatalysts: Environmental Purification and Energy Conversion. In *Development of g-C3N4-Based Photocatalysts: Environmental Purification and Energy Conversion*. DOI: 10.3390/books978-3-0365-9660-0.

Copyright © 2026, ISSN 1978-2993

[70]. Moharana, S., Sahu, B.B., Nayak, R., Mahaling, R.N. (2022). 8 - Synthesis and properties of percolative metal oxide-polymer composites. In: Haider, S., Haider, A. (eds) *Renewable Polymers and Polymer-Metal Oxide Composites*. Elsevier, pp. 253–282. DOI: 10.1016/B978-0-323-85155-8.00001-7.

[71]. Kim, M.G., Kang, J.M., Lee, J.E., Kim, K.S., Kim, K.H., Cho, M., Lee, S.G. (2021). Effects of Calcination Temperature on the Phase Composition, Photocatalytic Degradation, and Virucidal Activities of TiO2 Nanoparticles. *ACS Omega*, 6(16), 10668–10678. DOI: 10.1021/acsomega.1c00043.

[72]. Abeysinghe, J.P., Gillan, E.G. (2023). Chapter 2 - Thermochemical reaction strategies for the rapid formation of inorganic solid-state materials. In: House, J.E. (ed) *Dynamic Processes in Solids*. Elsevier, pp. 51–95. DOI: 10.1016/B978-0-12-818876-7.00005-2.

[73]. Benchikhi, M., El Ouatib, R., Guillemet-Fritsch, S., Er-Rakho, L., Durand, B., Kassmi, K. (2015). Influence of chelating agent on the morphological properties of α-CuMoO4 powder synthesized by sol–gel method. *Journal of Materials and Environmental Science*, 6(12), 3470–3475.

[74]. Kessaratikoon, T., Saengsaen, S., Del Gobbo, S., D'Elia, V., Sooknoi, T. (2022). High Surface Area ZnO-Nanorods Catalyze the Clean Thermal Methane Oxidation to CO2. *Catalysts*, 12(12) DOI: 10.3390/catal12121533.

[75]. Tanaka, S. (2019). Solid State Reactions and Sintering. In: Hojo, J. (eds) *Materials Chemistry of Ceramics*. Springer, Singapore. pp. 45–74. DOI: 10.1007/978-981-13-9935-0_3.

[76]. Krisha, S., Menaka, S., Celshia, S., Selvamani, M., Suresh, V. (2024). Synthesis of Copper Molybdate and Its Electrochemical Sensing of Paracetamol. *Cureus*, 16, e63925. DOI: 10.7759/cureus.63925.

[77]. Rondinini, S., Ardizzone, S., Cappelletti, G., Minguzzi, A., Vertova, A. (2009). Materials | Sol–Gel Synthesis. In: Garche, J. (ed) *Encyclopedia of Electrochemical Power Sources*. Amsterdam: Elsevier, pp. 613–624. DOI: 10.1016/B978-044452745-5.00054-X.

[78]. Saikumari, N., Dev, S.M., Dev, S.A. (2021). Effect of calcination temperature on the properties and applications of bio extract mediated titania nano particles. *Scientific Reports*, 11(1), 1734. DOI: 10.1038/s41598-021-80997-z.

[79]. Muñoz-Flores, P., Poon, P.S., Sepulveda, C., Ania, C.O., Matos, J. (2022). Photocatalytic performance of carbon-containing cumo-based catalysts under sunlight illumination. *Catalysts*, 12(1), 46. DOI: 10.3390/catal12010046/S1.

[80]. Ramesh, M. (2021). CuO as efficient photo catalyst for photocatalytic decoloration of wastewater containing Azo dyes. *Water Practice and Technology*, 16(4), 1078–1090. DOI: 10.2166/wpt.2021.067.

[81]. Ghorai, T.K., Dhak, D., Dalai, S., Pramanik, P. (2008). Effect of photocatalytic activities of nano-sized copper molybdate (CuMoO4)-doped bismuth titanate (Bi2Ti4O11) (CMBT) alloy. *Materials Research Bulletin*, 43(7), 1770–1780. DOI: 10.1016/j.materresbull.2007.07.009.

Copyright © 2026, ISSN 1978-2993